

MOA-2015-BLG-337: A PLANETARY SYSTEM WITH A LOW-MASS BROWN DWARF/PLANETARY
BOUNDARY HOST, OR A BROWN DWARF BINARY

S. MIYAZAKI^{†,1,2} T. SUMI,^{1,2} D. P. BENNETT,^{3,4,2} A. GOULD,^{5,6,7,8} A. UDALSKI,^{9,10} I. A. BOND,^{11,2} N. KOSHIMOTO,^{1,2}
M. NAGAKANE,^{1,2} AND N. RATTENBURY^{12,2}

F. ABE,¹³ A. BHATTACHARYA,^{3,4} R. BARRY,⁴ M. DONACHIE,¹² A. FUKUI,¹⁴ Y. HIRAO,¹ Y. ITOW,¹⁵ K. KAWASAKI,¹
M. C. A. LI,¹² C. H. LING,¹¹ Y. MATSUBARA,¹⁵ T. MATSUO,¹ Y. MURAKI,¹⁵ K. OHNISHI,¹⁶ C. RANC,⁴ T. SAITO,¹⁷
A. SHARAN,¹² H. SHIBAI,¹ H. SUEMATSU,¹ D. SUZUKI,¹⁸ D.J. SULLIVAN,¹⁹ P. J. TRISTRAM,²⁰ T. YAMADA,¹ AND
A. YONEHARA²¹

(MOA COLLABORATION)

S. KOZŁOWSKI,⁹ P. MRÓZ,⁹ M. PAWLAK,⁹ R. POLESKI,²² P. PIETRUKOWICZ,⁹ J. SKOWRON,⁹ I. SOSZYŃSKI,⁹
M. K. SZYMAŃSKI,⁹ AND K. ULACZYK⁹

(OGLE COLLABORATION)

M. D. ALBROW,²³ S.-J. CHUNG,^{5,24} C. HAN,²⁵ Y. K. JUNG,⁵ K.-H. HWANG,⁵ Y.-H. RYU,²⁶ I.-G. SHIN,²⁷
Y. SHVARTZVALD,^{28,29} J. C. YEE,²⁷ W. ZANG,^{30,31} W. ZHU,³² S.-M. CHA,^{5,33} D.-J. KIM,⁵ H.-W. KIM,⁵ S.-L. KIM,^{5,24}
C.-U. LEE,^{5,24} D.-J. LEE,⁵ Y. LEE,^{5,33} B.-G. PARK,^{5,24} AND R. W. POGGE⁶

(KMTNET COLLABORATION)

¹Department of Earth and Space Science, Graduate School of Science, Osaka University, 1-1 Machikaneyama, Toyonaka, Osaka 560-0043, Japan

²MOA collaboration

³Department of Physics, University of Notre Dame, Notre Dame, IN 46556, USA

⁴Laboratory for Exoplanets and Stellar Astrophysics, NASA/Goddard Space Flight Center, Greenbelt, MD 20771, USA

⁵Korea Astronomy and Space Science Institute, Daejeon 34055, Korea

⁶Department of Astronomy Ohio State University, 140 W. 18th Ave., Columbus, OH 43210, USA

⁷Max-Planck-Institute for Astronomy, Königstuhl 17, 69117 Heidelberg, Germany

⁸KMTNet collaboration

⁹Warsaw University Observatory, Al. Ujazdowskie 4, 00-478 Warszawa, Poland

¹⁰OGLE collaboration

¹¹Institute of Information and Mathematical Sciences, Massey University, Private Bag 102-904, North Shore Mail Centre, Auckland, New Zealand

¹²Department of Physics, University of Auckland, Private Bag 92019, Auckland, New Zealand

¹³Institute for Space-Earth Environmental Research, Nagoya University, Nagoya 464-8601, Japan

¹⁴Okayama Astrophysical Observatory, National Astronomical Observatory, 3037-5 Honjo, Kamogata, Asakuchi, Okayama 719-0232, Japan

¹⁵Institute for Space-Earth Environmental Research, Nagoya University, Nagoya, 464-8601, Japan

¹⁶Nagano National College of Technology, Nagano 381-8550, Japan

¹⁷Tokyo Metropolitan College of Industrial Technology, Tokyo 116-8523, Japan

¹⁸Institute of Space and Astronautical Science, Japan Aerospace Exploration Agency, 3-1-1 Yoshinodai, Chuo, Sagami, Kanagawa 252-5210, Japan

¹⁹School of Chemical and Physical Sciences, Victoria University, Wellington, New Zealand

²⁰University of Canterbury Mt. John Observatory, P.O. Box 56, Lake Tekapo 8770, New Zealand

²¹Department of Physics, Faculty of Science, Kyoto Sangyo University, Kyoto 603-8555, Japan

²²Department of Astronomy, Ohio State University, 140 W. 18th Ave., Columbus, OH 43210, USA

²³University of Canterbury, Department of Physics and Astronomy, Private Bag 4800, Christchurch 8020, New Zealand

²⁴Korea University of Science and Technology, 217 Gajeong-ro, Yuseong-gu, Daejeon, 34113, Korea

²⁵Department of Physics, Chungbuk National University, Cheongju 28644, Republic of Korea

²⁶*Korea Astronomy and Space Science Institute, Daejeon 34055, Republic of Korea*

²⁷*Harvard-Smithsonian Center for Astrophysics, 60 Garden St., Cambridge, MA 02138, USA*

²⁸*Jet Propulsion Laboratory, California Institute of Technology, 4800 Oak Grove Drive, Pasadena, CA 91109, USA*

²⁹*NASA Postdoctoral Program Fellow*

³⁰*Physics Department and Tsinghua Centre for Astrophysics, Tsinghua University, Beijing 100084, China*

³¹*Department of Physics, Zhejiang University, Hangzhou, 310058, China*

³²*Canadian Institute for Theoretical Astrophysics, University of Toronto, Toronto, ON M5S 3H8, Canada*

³³*School of Space Research, Kyung Hee University, Yongin, Kyeonggi 17104, Korea*

Submitted to Apj

ABSTRACT

We report the discovery and the analysis of the short timescale binary-lens microlensing event, MOA-2015-BLG-337. The lens system could be a planetary system with a very low mass host, around the brown dwarf/planetary mass boundary, or a brown dwarf binary. We found two competing models that explain the observed light curves with companion/host mass ratios of $q \sim 0.01$ and ~ 0.17 , respectively. From the measurement of finite source effects in the best-fit planetary model, we find a relatively small angular Einstein radius of $\theta_E \simeq 0.03$ mas which favors a low mass lens. We conduct a Bayesian analysis to obtain the probability distribution of the lens properties. The results for the planetary models strongly depend on the minimum mass, M_{\min} , in the assumed mass function. In summary, there are two solutions of the lens system: (1) a brown dwarf/planetary mass boundary object orbited by a super-Neptune (the planetary model with $M_{\min} = 0.001M_{\odot}$) and (2) a brown dwarf binary (the binary model). If the planetary models is correct, this system can be one of a new class of planetary system, having a low host mass and also a planetary mass ratio ($q < 0.03$) between the host and its companion. The discovery of the event is important for the study of planetary formation in very low mass objects. In addition, it is important to consider all viable solutions in these kinds of ambiguous events in order for the future comprehensive statistical analyses of planetary/binary microlensing events.

Keywords: microlensing — exoplanets — brown dwarfs

1. INTRODUCTION

Exoplanets and brown dwarfs (BDs) are usually inferred from indirect methods owing to their intrinsic faintness. Each method has its own unique sensitivity range and can probe different regions of the planet parameter space. Gravitational microlensing has a unique sensitivity to planets with masses down to Earth-mass orbiting just outside of the snow line (Mao & Paczynski 1991; Gould & Loeb 1992), beyond which giant planets can efficiently form according to the core accretion theory (Pollack et al. 1996; Kokubo & Ida 2002), while the radial velocity (RV) (Butler et al. 2006; Mayor & Queloz 1995) and transit methods (Borucki et al. 2011; Batalha et al. 2013) are mostly sensitive to planets that are relatively more massive or orbit closer to their host stars.

Searching for companions to BDs is very important to understand the formation of BDs. Though still a matter of debate, most theories suppose that BDs were formed by the direct collapse of molecular clouds on a much smaller scale than stars, and promoted by turbulent fragmentation (Luhman 2012). Some young BDs are observed surrounded by disks of material (Luhman et al. 2005; Apai et al. 2005; Ricci et al. 2012). The recent direct imaging survey to search for very low mass stars (VLMS) and BDs found a strong preference to equal mass binary systems if they have companions (Liu et al. 2010; Burgasser et al. 2006). Burgasser et al. (2006) found a very steep index $\gamma = 4.2 \pm 1.0$ for a power-law distribution $\propto q^\gamma$, which is derived by fitting the observed mass ratio distribution. Though there are still large uncertainties because the masses of the objects detected by direct imaging were estimated based on assumed ages, lower mass ratio (i.e., $q \leq 0.3$) binaries would be very uncommon among field VLMS and BDs. However, there have been several discoveries of binary BDs (Han et al. 2017) as well as a BD orbiting an M dwarf (Han et al. 2016) with small mass ratios ($q < 0.3$) by microlensing. In addition, Han et al. (2013) reported the discovery of a system composed of a planetary-mass object with $1.9 \pm 0.2 M_{\text{Jup}}$ orbiting a BD at a projected separation of 0.89 ± 0.03 AU, and suggested that the companion may have formed in a proto-planetary disk around the BD host. Microlensing can play an important role for understanding the formation of VLMS and BDs by detecting companions of low-mass hosts.

Microlensing surveys and follow-up groups have contributed to finding several dozen exoplanets around M-dwarf stars, revealing that low-mass planets are much more common than massive ones beyond the snow line (Gould et al. 2010; Sumi et al. 2010; Cassan et al. 2012; Shvartzvald et al. 2016; Suzuki et al. 2016). Particularly, Suzuki et al. (2016) and Udalski et al. (2018) found a possible peak in the mass ratio function and suggested that cold Neptunes would be the most common planets beyond the snow line. This is qualitatively consistent with predictions from core accretion theory. However, the observed abundance of ice and gas giant planets is an order of magnitude more than that predicted by the formation models around M-dwarf stars. However, since gas-giant planets are composed mainly of hydrogen and helium that would be removed from their proto-planetary disk in a few million years, massive Jovian planets are unlikely to be formed around low-mass stars like M-dwarfs or even BDs due to the lack of planet-forming material (Ida & Lin 2005).

Without an observed microlensing parallax, we cannot determine the absolute masses of the host star and planet from a microlensing light curve alone. In such cases, a Bayesian analysis is usually applied by using Galactic model priors (comprising a stellar mass function and number density, and velocity distributions) to obtain the posterior probability distributions of the physical parameters of the lens system. The results of the Bayesian analysis generally strongly depend on the priors. In addition, special attention must be paid to low mass host stars because the mass function of low mass objects like brown dwarfs or even smaller mass objects down to planetary mass is very uncertain. Gravitational microlensing plays an important role for studying the occurrence of planets in very wide orbits and planetary mass objects unbound to any host stars. By investigating the time scale distribution of short microlensing events in the MOA dataset in 2006-2007, Sumi et al. (2011) suggested a possible population of unbound or distant Jupiter-mass objects. Unbound planets are expected from various processes, including planet-planet scattering (Levison et al. 1998; Ford & Rasio 2008; Guillochon et al. 2011), star-planet scattering (Holman & Wiegert 1999; Musielak et al. 2005; Doolin & Blundell 2011; Malmberg et al. 2011; Veras & Raymond 2012; Kaib et al. 2013) and stellar mass loss and death (Veras et al. 2011; Veras & Tout 2012; Voyatzis et al. 2013). Mróz et al. (2017) recently updated the study with a larger sample and reported no significant excess of short-timescale (1-2 days) microlensing events and placed 95% upper limits on the frequency of unbound or distant Jupiter mass objects of 0.25 planet per main sequence star using

the OGLE 2010-2015 observations. They also reported a possible large population of unbound or distant super-Earth mass objects (Dai & Guerras 2018). These studies have played an important role to constrain the mass function of low-mass objects, while it is still uncertain.

In this paper, we report the discovery and present the analysis of the short-timescale binary microlensing event, MOA-2015-BLG-337. We find two competing models that explain the observed data. One comprises a planetary mass-ratio lens system and the other, a binary mass ratio lens system. Because of the short time scale, ~ 6 days, of this event, we conducted our Bayesian analysis with an assumed mass function extending down to brown dwarf and also down to planetary mass regimes. The rest of this paper is organized as follows. We describe the observation and the data sets in Section 2, and in Section 3 we present our light curve model. In Section 4, we present the calibration of the source star and an estimation of the angular Einstein radius. In Section 5, we present a Bayesian analysis in order to estimate the physical parameters of the lens system. Finally, we present our conclusions in Section 6 and discussion in Section 7.

2. OBSERVATION

The second phase of the MOA (The Microlensing Observations in Astrophysics; Bond et al. 2001; Sumi et al. 2003) collaboration, MOA-II, conducts a high cadence microlensing exoplanet survey toward the Galactic bulge using the 1.8 m MOA-II telescope equipped with a very wide 2.2 deg^2 field of view (FOV) CCD camera, MOA-cam3 (Sako et al. 2008) at Mount John University Observatory (MJUO) in New Zealand. The six MOA-II fields ($\sim 13 \text{ deg}^2$) with the highest lensing rate are observed with a 15 minute cadence, while the next six best fields are observed with a 47 minute cadence, and eight additional fields are observed with a 95 minute cadence. Most MOA-II observations use the custom MOA-Red wide band filter, which corresponds to the sum of the standard Cousins *R*- and *I*-bands. MOA-II issues ~ 600 microlensing event alerts in real time each year.¹ Event MOA-2015-BLG-337 was first discovered on 2015 July 10 UT ($\text{HJD}' \equiv \text{HJD} - 2450000 = 7214$) and positioned at $(\text{RA}, \text{Dec})_{\text{J2000}} = (18^{\text{h}}07^{\text{m}}47^{\text{s}}.69, -28^{\circ}10'13''.00)$, which corresponds to Galactic coordinates $(l, b) = (3.11^{\circ}, -3.83^{\circ})$. The event was located in field “gb14”, which has been regularly observed and monitored with a 15 minute cadence by MOA.

The Optical Gravitational Lensing Experiment (OGLE; Udalski et al. 2015) also conducts a microlensing survey toward the Galactic bulge by using the 1.3 m Warsaw telescope at the Las Campanas Observatory in Chile. The fourth phase of OGLE, OGLE-IV, started observations in 2010 with a 1.4 deg^2 FOV mosaic CCD camera. OGLE observes bulge fields with cadences ranging from every 20 minutes for three central fields to less than once every night for the outer bulge fields. Most observations are taken in the standard Kron-Cousin *I*- band with occasional observations in the Johnson *V*-band. OGLE-IV issues ~ 2000 microlensing event alerts in real time each year.² OGLE independently found and alerted the event as OGLE-2015-BLG-1598 on 2015 July 11 UT ($\text{HJD}' = 7215$).

The MOA observers noticed that the light curve of the MOA-2015-BLG-337 deviated from a single-lens model around $\text{HJD}' \sim 7214.9$ and the MOA collaboration issued an anomaly alert encouraging follow-up observations. A member of modelers immediately modeled this event and found two indistinguishable solutions with planetary and binary lens mass ratios. The KMTNet (Korea Microlensing Telescope Network; Kim et al. 2016) also observed this event as KMT-2015-BLG-0511 (Kim et al. 2018) in their regular observation survey with their three 1.6 m KMTNet telescopes at CTIO, SAAO and SSO. KMTNet-CTIO and OGLE light curves also cover the part of the anomaly. This event was also observed by the 0.61 m Boller & Chivens telescope at MJUO. The number of data points of each telescope and passband are shown in Table 1. The MOA and B&C images were reduced with MOA’s implementation (Bond et al. 2001) of the difference image analysis (DIA) method (Tomaney & Crofts 1996; Alard & Lupton 1998; Alard 2000). The OGLE data were reduced with the OGLE DIA (Wozniak 2000) photometry pipeline (Udalski et al.

¹ <https://www.massey.ac.nz/iabond/moa/alerts/>

² <http://ogle.astrouw.edu.pl/ogle4/ews/ews.html>

2015). The KMTNet data also were reduced with their PySIS photometry pipeline (Albrow et al. 2009; Kim et al. 2016).

The photometric errors estimated from pipelines are generally underestimated in such high stellar density fields like in the Galactic bulge. We, therefore, renormalized the error bars of the individual datasets following the method described in Yee et al. (2012), i.e., $\sigma'_i = k\sqrt{\sigma_i^2 + e_{\min}^2}$, where σ_i is the original error bar of the i -th data points in magnitude, k and e_{\min} are re-normalizing parameters. The value of e_{\min} represents systematic errors that dominates at high magnification and can be affected by flat-fielding errors. First, we fit the light curve to find a tentative best-fit model. Then, we set $e_{\min} = 0.03$ and selected k value so that the cumulative χ^2 distribution from the tentative best model sorted by model-magnification is close to linear with a slope of 1 and $\chi^2/d.o.f. \sim 1$ as shown in Table 1. The coefficients applied for the OGLE- I data are consistent with those taken from Skowron et al. (2016). After the error renormalization, we fitted the light curve again to find the final best model. In general, error renormalization processes do not significantly affect the final results. We confirmed the final best model is consistent with the previous best model before error renormalization.

The light curve of the event is shown in Figure 1. It shows a clear asymmetric feature, which cannot be explained by a standard point-source point-lens (PSPL) model. We describe the procedure of binary-lens modeling in the following section.

3. LIGHT CURVE MODELS

3.1. Model Description

There are seven fitting parameters in a standard binary lens modeling; the time when the source is closest to a reference point, t_0 ; the Einstein radius crossing time, $t_E = \theta_E/\mu_{\text{rel}}$, where θ_E and μ_{rel} are the angular Einstein radius and the lens-source relative proper motion, respectively; the impact parameter, u_0 , in units of Einstein radius, R_E ; the mass ratio of binary components, q ; the projected separation between binary components in units of R_E , s ; the angle of the source trajectory with respect to the binary lens axis, α ; and finally the ratio of the angular source star size to angular Einstein radius $\rho \equiv \theta_*/\theta_E$, where θ_* is the angular source radius. If ρ is measured from the light curve modeling, we can determine the angular Einstein radius, $\theta_E = \theta_*/\rho$, because the source angular radius, θ_* can be estimated from its de-reddened color and extinction-free apparent magnitude (Boyajian et al. 2014). Given parameters $\mathbf{x} = (t_E, t_0, u_0, q, s, \alpha, \rho)$, the magnification $A(t, \mathbf{x})$ can be calculated at any given time, t . The model light curve can be written as :

$$F(t) = A(t, \mathbf{x})f_s + f_b, \quad (1)$$

where f_s is the un-magnified source flux, and f_b is the blend flux. Each telescope and pass-band has a corresponding f_s , f_b pair. We use a linear limb-darkening model for the surface brightness of the source star, $I(\theta) = I(0)[1 - u_\lambda(1 - \cos\theta)]$, where θ is the angle between the normal to the stellar surface and the line of sight, and u_λ is the limb-darkening coefficient. We estimated the effective temperature of the source, $T_{\text{eff}} \sim 6000\text{K}$, and assumed a metallicity, $\log[M/H] = 0.0$ and surface gravity $\log(g/\text{cm s}^{-1}) = 4.50$. According to the ATLAS model by Claret & Bloemen (2011), the limb-darkening coefficients are $u_R = 0.7021$, $u_I = 0.6055$ and $u_V = 0.7801$. The u_{R+I} value, corresponding to limb darkening in the MOA-*Red* passband, is calculated as the mean of u_R and u_I .

3.2. Modeling

We fitted the light curve by using a Markov Chain Monte Carlo (MCMC) approach (Verde et al. 2003) and our implementation of the image-centered ray-shooting method (Bennett & Rhie 1996; Bennett 2010). At first, we conducted a global grid search by using the standard static binary lens model with 9,680 fixed grid points covering wide ranges of the three parameters, q , s and α , with all other parameters allowed to vary. Then, the best 100 models with the smallest χ^2 were refined by allowing all parameters to vary. With this procedure, we can find the best fit model without missing any local minimum solutions across the wide range of parameter space. We found a pair of optimal solutions, one with a planetary mass ratio of $q \sim 1.1 \times 10^{-2}$ and the other with a stellar binary mass ratio of $q \sim 1.7 \times 10^{-1}$. These parameters are labeled as ‘‘Planetary’’ and ‘‘Binary’’ in Table 2, respectively. We could not find any model with a significant microlensing parallax effect as expected because of the short event time scale.

In addition, we examined the possibility of a binary-source point-lens (BSPL) model for this event, and confirmed it could be ruled out by $\Delta\chi^2 > 50$.

In the planetary model, there are two statistically indistinguishable solutions, one with a close ($s < 1$) binary separation and the other with a wide ($s > 1$) separation. The close model is favored by only $\Delta\chi^2 \simeq 0.2$. This severe degeneracy between s and s^{-1} , which is known as close/wide degeneracy, is common for central caustic crossing events because the shapes of the central-caustic with s and s^{-1} are similar for smaller q (Griest & Safizadeh 1998; Dominik 1999). In these planetary models, the finite source effect with $\rho \sim 2 \times 10^{-2}$ is detected with $\Delta\chi^2 > 35$ compared to the point source models, and the signal mostly came from MOA-Red data. This ρ value is relatively large compared to the typical values for other microlensing planetary events and it indicates a small angular Einstein radius, θ_E , and prefers a smaller lens mass in the Bayesian analysis of Section 5.

In the binary model, the model deviates from the planetary model particularly between $7214.5 < \text{HJD} - 2450000 < 7214.8$ (see Figure 1). The difference between these models is only $\Delta\chi^2 \sim 6$ due to the large photometric uncertainties in this period. There is also a close/wide degeneracy in the binary model: the close model is favored over the wide one by $\Delta\chi^2 \sim 2$. The finite source effect was not significantly detected for these binary models, showing only an improvement of $\chi^2 < 4.0$ compared to the point source model. Thus, we do not adopt the best-fit ρ value but put only an upper limit on ρ in the following analysis.

Our inability to distinguish between the planetary and binary models in this event is due to the poor coverage of the anomalous part of the light curve where there are only subtle differences in the magnification pattern between these models. Figure 2 represents the caustic geometries and the magnification patterns around them for each model. The magnification pattern this event can be explained by the two different central caustic shapes, which makes it difficult to distinguish the two planetary and stellar binary solutions. Similar to this event, there are a number of microlensing events which can be explained with both stellar binary and planetary mass ratio lens systems (Gaudi & Han 2004; Choi et al. 2012; Park et al. 2014).

4. ANGULAR EINSTEIN RADIUS

By using the measurement of ρ ($= \theta_*/\theta_E$) from the light curve, the source star angular radius θ_* allows us to estimate θ_E . We can empirically estimate θ_* from its intrinsic magnitude and color (Boyajian et al. 2014).

We converted the instrumental source magnitude in MOA-Red and MOA-V bands into the standard Kron-Cousin I -band and Johnson V -band scales using the model light curve. Following the procedure described in Bond et al. (2017), we cross-referenced stars within $2'$ around the source star between MOA star catalog reduced by DoPHOT (Schechter et al. 1993) and the OGLE-III photometry map (Szymański et al. 2011). We found the following relations,

$$\begin{aligned} I_{\text{OGLE-III}} - R_{\text{MOA}} &= (28.119 \pm 0.005) - (0.206 \pm 0.002)(V - R)_{\text{MOA}} \\ V_{\text{OGLE-III}} - V_{\text{MOA}} &= (27.901 \pm 0.005) - (0.148 \pm 0.002)(V - R)_{\text{MOA}}. \end{aligned}$$

In order to correct interstellar extinction and reddening, we followed the standard procedure in Yoo et al. (2004), which uses the Red Clump Giants (RCG) in the color-magnitude diagrams (CMD) as standard candles. Figure 3 shows the OGLE-III CMD within $2'$ around the source star, plotted over the CMD of stars in Baade's window observed by the HST (Holtzman et al. 1998) whose extinction and reddening are matched by using RCG position. The magnitude and color of source and the center of the RCG, $(V - I, I)_s = (1.611, 19.682) \pm (0.019, 0.012)$ and $(V - I, I)_{\text{RCG}} = (2.050, 15.553) \pm (0.013, 0.048)$ are shown as filled blue and red circles, respectively. We obtained the intrinsic RCG centroid in this field $(V - I, I)_{\text{RCG},0} = (1.060, 14.348) \pm (0.070, 0.040)$ (Bensby et al. 2013; Nataf et al. 2013), and found the extinction and reddening of RCG centroid to be $A_{I,\text{RCG}} = 1.205 \pm 0.062$ and $E(V - I)_{\text{RCG}} = 0.990 \pm 0.071$, respectively. Assuming the source suffered the same extinction and reddening as the bulge RCGs in the field, the extinction-free source magnitude and color values are $(V - I, I)_{s,0} = (0.621, 18.478) \pm (0.074, 0.064)$. From the CMD, we can see that the source star is slightly bluer than other typical bulge dwarf stars in this field. This is possibly because the source does not have the same extinction as the median of the red clump stars. However, even if we assume 10% less extinction and reddening from those for the median RCG, the changes in the θ_E and μ_{rel} are less

than 3%, which is much less than the typical uncertainty of these values. We summarize the color, magnitude and angular radius of the source star in Table 3. We also independently obtained the intrinsic source color using a linear regression from KMTNet-CTIO I and V , $(V - I)_{s,0,KMTNet} = 0.688 \pm 0.066$, which is consistent with the color from MOA-Red and V above but with a smaller uncertainty. We adopt this $(V - I)_{s,0,KMTNet}$ in the following analysis.

We estimated the source angular radius by using following empirical relation,

$$\log \theta_{LD} = 0.5014 + 0.4197(V - I) - 0.2I, \quad (2)$$

where $\theta_{LD} \equiv 2\theta_*$ (Fukui et al. 2015). This relation is derived by using a subsample of FGK stars between $3900\text{K} < T_{\text{eff}} < 7000\text{K}$ from Boyajian et al. (2014) and the accuracy of this relation is better than 2%. According to this relation, we found that $\theta_* \equiv \theta_{LD}/2 = 0.621 \pm 0.045 \mu\text{as}$, and angular Einstein radius θ_E and the lens-source relative proper motion μ_{rel} are given as,

$$\theta_E = \frac{\theta_*}{\rho} = \begin{cases} 0.028 \pm 0.004 \text{ mas (for the planetary close model)} \\ 0.024 \pm 0.003 \text{ mas (for the planetary wide model)} \\ > 0.034 \text{ mas (for the binary close model)} \\ > 0.035 \text{ mas (for the binary wide model)} \end{cases}$$

$$\mu_{\text{rel}} = \frac{\theta_E}{t_E} = \begin{cases} 1.90 \pm 0.29 \text{ mas yr}^{-1} \text{ (for the planetary close model)} \\ 1.59 \pm 0.18 \text{ mas yr}^{-1} \text{ (for the planetary wide model)} \\ > 2.26 \text{ mas yr}^{-1} \text{ (for the binary close model)} \\ > 2.11 \text{ mas yr}^{-1} \text{ (for the binary wide model),} \end{cases}$$

where only the lower limits are given for the binary models.

5. BAYESIAN ANALYSIS

Since no significant parallax signal is detected in this event, we cannot directly measure the lens properties, the host mass, M_{host} , the distance, D_L or lens-source relative transverse velocity, v_{\perp} . Therefore, we conducted a Bayesian analysis to obtain the probability distribution of the lens properties (Beaulieu et al. 2006; Gould et al. 2006; Bennett et al. 2008). We assumed the Galactic model (Han & Gould 1995) as the priors for Galactic mass density and velocity. The observed t_E and θ_E can constrain the lens physical parameters in the Bayesian analysis. Both the observed t_E and θ_E value in this event are smaller than average. This suggests that the host mass is likely to be very low because both t_E and θ_E are proportional to \sqrt{M} . Therefore, we need a mass function extending to a very low mass regime in the Bayesian analysis. We adopt the broken power-law mass function used in Sumi et al. (2011) and Mróz et al. (2017) as follows,

$$dN/dM = \begin{cases} a_1 M^{-\alpha_{\text{bd}}} & (M_{\text{min}} \leq M/M_{\odot} \leq 0.08) \\ a_2 M^{-\alpha_{\text{ms2}}} & (0.08 \leq M/M_{\odot} \leq M_{\text{break}}) \\ a_3 M^{-\alpha_{\text{ms1}}} & (M_{\text{break}} \leq M/M_{\odot} \leq 1.0), \end{cases} \quad (3)$$

where $\alpha_{\text{ms1}} = 2.0$ and $\alpha_{\text{ms2}} = 1.3$ are the power-law indexes for main sequence stars. We adopt the power-law index for the brown dwarfs of $\alpha_{\text{bd}} = 0.49$ with $M_{\text{break}} = 0.7$ (Sumi et al. 2011) and $\alpha_{\text{bd}} = 0.8$ with $M_{\text{break}} = 0.5$ (Mróz et al. 2017). Mróz et al. (2017) found that the mass function with the minimum mass of $M_{\text{min}} = 0.01$ is consistent with the observed event time scale distribution. Below $M/M_{\odot} < 0.01$, they found the upper limit of the abundance of Jupiter mass objects is 0.25 per star with 95% confidence, while the lower limit of the mass function is not well constrained. Thus, we applied $M_{\text{min}} = 0.01$ and 0.001 in order to see how the results depend on the assumed mass functions in this range. In these mass functions, the relative fractions of number densities between main sequence stars, brown dwarfs and planetary mass objects are 1:0.72:0.27 and 1:0.99:0.71, respectively. We also assume that probability of a lens primary to host a companion with the measured mass ratio at a separation of $\sim R_E$ is independent of the host mass.

Here the model with $(\alpha_{\text{bd}}, M_{\text{min}}) = (0.49, 0.001)$ has 0.27 planetary mass objects per main sequence stars, which is just slightly higher than the 95% upper limit of Jupiter-mass planetary mass objects of Mróz et al. (2017). Thus, the abundance of planetary-mass objects in this model can be considered as an upper limit. On the other hand, the model with $(\alpha_{\text{bd}}, M_{\text{min}}) = (0.8, 0.001)$ has even more planetary-mass objects, thus it can be considered as an extreme case.

The lens parameters and the probability distributions of the lens properties derived from our Bayesian analysis are given in Tables 4 and 5 and Figures 4 and 5. We combined the probability distribution of the close and wide models by weighting the probability distribution of the wide models by $e^{-\Delta\chi^2/2}$, where $\Delta\chi^2 = \chi_{\text{wide}}^2 - \chi_{\text{close}}^2$. However, the probability distribution of the projected separation between the host and the companion r_{\perp} for the binary model is not combined because the difference of the s values between the close and wide models are so large, $s_{\text{wide}}/s_{\text{close}} \simeq 18$, compared to that value of the planetary models of $\simeq 2.5$.

As one can see in these tables, the results do not depend strongly on the value of α_{bd} . However, the host mass for the planetary model strongly depends on the assumed M_{min} . For the planetary models with $M_{\text{min}} = 0.01$, the lens system is likely a brown dwarf orbited by a Saturn mass giant planet. The lens masses for the planetary models with $M_{\text{min}} = 0.001M_{\odot}$ are lower than that with $M_{\text{min}} = 0.01M_{\odot}$ as expected, but consistent to within 1σ . This is because of the strong restrictions from the observed values of t_{E} and θ_{E} . In the planetary models with $M_{\text{min}} = 0.001$, the host, which is on the boundary between a super giant planetary mass object and a very low-mass brown dwarf, is orbited by a super Neptune-mass planet or a sub-Saturn-mass planet. The assumption of $M_{\text{min}} = 0.01$, i.e., the sharp cut-off in the lens mass function at $0.01M_{\odot}$ seems unphysical because there are many claims of brown dwarfs with masses below $0.01M_{\odot}$. Thus, we do not consider this model as a final result but as a reference for comparison. For the binary model, on the other hand, the dependency of the Bayesian results on M_{min} is not strong. This is because we only have a lower limit on θ_{E} , thus a relatively more massive host is allowed in the Bayesian analysis. This model indicates that the lens system is a brown dwarf binary with a small mass ratio. In addition, we conducted the independent Bayesian analysis with a different Galactic model by using the same procedure as Bennett et al. (2014). We confirmed that the results of the Bayesian analysis were consistent with those in Table 4 and 5. We found that the derived lens-source proper motion, μ , for the binary solutions is preferred than that of the planetary solutions by the Galactic model prior. However, this preference is not so large compared to the preference of the planetary model by the $\Delta\chi^2 \sim 6$ from the light curve fitting. So, we concluded that this event has an ambiguity between two solutions while the planetary solution is slightly preferred.

6. SUMMARY AND CONCLUSIONS

We analyzed the microlensing event MOA-2015-BLG-337 and found there exist two very degenerate solutions with mass ratios of $q \sim 10^{-2}$ and $q \sim 10^{-1}$. The former planetary solutions are favored over the latter binary solution by $\Delta\chi^2 \sim 6$. There are degeneracies between the close and the wide solutions with $\Delta\chi^2 \simeq 0.2$ and $\Delta\chi^2 \simeq 2.0$ in the planetary and the binary models, respectively. We could measure the finite source effect for only the planetary models and obtained a large value of $\rho \sim 10^{-2}$ implying a very low mass lens. We could not detect a clear microlens parallax signal in the light curve. Therefore, we conducted a Bayesian analysis by using the observed t_{E} and θ_{E} values in order to estimate the probability distribution of the physical properties of the lens system. Since the host is likely to have a lower mass than main sequence stars, we used a mass function extending to brown dwarf and planetary masses as a prior. The Bayesian results for both planetary and binary models do not depend greatly on the value of α_{bd} . The results for the binary model do not depend on the chosen value of M_{min} . On the other hand, the results for planetary models strongly depend on the minimum mass of M_{min} , while the results are consistent with each other within 1σ . So, there are two competing models of the lens system: (1) a brown dwarf/planetary mass boundary object orbited by a super-Neptune (the planetary model with $M_{\text{min}} = 0.001M_{\odot}$) and (2) a brown dwarf binary (the binary model). Here we assumed that probability of a lens primary to host a companion with the measured mass ratio at a separation of $\sim R_{\text{E}}$ is independent of the mass of the host because we do not have any information on this.

7. DISCUSSION

Figure 6 shows the distribution of known bound exoplanets and very low mass companions in the plane of the host and companion masses. The two solutions for this event are shown by purple circles. The red and green circles indicate the planets found by microlensing, where filled and open circles indicates that their masses are directly measured or

estimated by a Bayesian analysis, respectively. The green circles indicate the microlensing binary events with large mass ratios of $q > 0.1$, which are brown-dwarf binaries or brown dwarfs orbiting around very low-mass M-dwarfs (Han et al. 2016; Jung et al. 2015; Choi et al. 2013; Han et al. 2017). They are likely formed by a different mechanism from that of planetary systems with $q < 0.03$. The binary model of this work belongs to this group. The favored planetary models can be one of a new class of planetary system, having an extremely low host mass and with a planetary mass ratio ($q < 0.03$). A similar system is MOA-2011-BLG-262L, where one of the models has a sub-Earth mass moon orbiting a gas giant primary (Bennett et al. 2014). And, Mróz et al. (2017) also found several short-timescale binary events which could have very low mass hosts. If such low host mass planetary systems exist, this offers a challenge to planet formation theory. However, the priors in our Bayesian analysis are highly uncertain at low masses for two reasons. First, the mass function in the low-mass region is highly uncertain, and second, we have no idea if the low mass objects are likely to host planetary mass ratio companions. Thus, we need to measure the lens mass and distance to know the abundances of planets in these low mass primaries.

In order to improve the situation to measure the physical parameters of such short-timescale microlensing events, firstly we have to get better data coverage and accuracy in the light curves to distinguish between competing models. Secondly, we can constrain the lens mass from the lens flux measurements through high resolution Adaptive Optics (AO) imaging from the ground or the HST directly. Although we will not be able to detect the flux from such a low mass object, we will be able to find upper limit constraints on the lens mass. Thirdly, the mass can be measured by observing microlensing parallax. Because annual significant parallax can not be measured in these short time scale events, we should attempt to measure the terrestrial parallax effect (Gould et al. 2009; Yee et al. 2009) as this would allow us to determine the lens mass directly from only the light curve when also combining finite source effects (Freeman et al. 2015). The small Einstein radius of the low mass object is suitable for observing this effect given the short baseline of observatories spread across the Earth’s surface. This would be implemented more frequently through improvements of microlensing surveys (Park et al. 2012) for rapid event identification and follow-up organization (Brown et al. 2013). Space-based parallax is more powerful for measuring the lens mass and this has been demonstrated by the simultaneous observations by the Spitzer satellite and ground-based telescopes (Gould & Yee 2014; Street et al. 2016).

In addition, we also advocate for the importance of considering all viable solutions in all ambiguous events which can be interpreted by both a planetary and a stellar binary lens system (Gaudi & Han 2004; Choi et al. 2012; Park et al. 2014; Hwang et al. 2018) in order to conduct comprehensive microlensing statistical analyses, such as that of Suzuki et al. (2016) and Udalski et al. (2018). Missing the solutions could lead to incorrect statistical results so that we should fully examine all the solutions in all microlensing events including ambiguous events, particularly in short-timescale events.

NASA’s WFIRST mission (Green et al. 2012; Spergel et al. 2013) will conduct a space-based microlensing survey toward the Galactic bulge in the near infrared and is planned to launch in mid 2020s. WFIRST fulfills all of these requirements with its high precision, high cadence and high spatial resolution survey. It is very sensitive to such short-timescale planetary events and will enable us to determine the lens masses directly using the space parallax. The PRIME (PRime-focus Infrared Microlensing Experiment) project is planning to conduct a microlensing survey toward the central region of the Galactic bulge ($|b| \leq 2\text{deg}$) in H -band by using a new 1.8m wide FOV telescope in South Africa. As the PRIME telescope can observe the same fields as WFIRST, simultaneously, the space-based parallax will be observed regularly without the current alert and follow-up strategy. The longer coverage of the PRIME survey can also add time series outside of the WFIRST’s observing window of 72 days duration. These future microlensing surveys will reveal the frequency of exoplanets around low-mass brown dwarfs and even the frequency of planetary mass objects orbited by exo-moons.

This research has made use of the KMTNet system operated by the Korea Astronomy and Space Science Institute (KASI) and the data were obtained at three host sites of CTIO in Chile, SAAO in South Africa, and SSO in Australia. The OGLE project has received funding from the National Science Centre, Poland, grant MAESTRO 2014/14/A/ST9/00121 to AU. Work by CR was supported by an appointment to the NASA Postdoctoral Program at the Goddard Space Flight Center, administered by USRA through a contract with NASA. Work by N.K. is supported by JSPS KAKENHI Grant Number JP15J01676. Work by Y.H. is supported by JSPS KAKENHI Grant Number

JP1702146. NTR is a Royal Society of New Zealand Rutherford Discovery Fellow. This work was supported by JSPS KAKENHI Grant Number JP17H02871. Work by C.H. was supported by the grant (2017R1A4A1015178) of National Research Foundation of Korea. Work by WZ, YKJ, and AG were supported by AST1516842 from the US NSF. WZ, IGS, and AG were supported by JPL grant 1500811.

REFERENCES

- Alard, C. 2000, *A&AS*, 144, 363
- Alard, C., & Lupton, R. H. 1998, *ApJ*, 503, 325
- Albrow, M. D., Horne, K., Bramich, D. M., et al. 2009, *MNRAS*, 397, 2099
- Apai, D., Pascucci, I., Bouwman, J., et al. 2005, *Science*, 310, 834
- Batalha, N. M., Rowe, J. F., Bryson, S. T., et al. 2013, *ApJS*, 204, 24
- Beaulieu, J.-P., Bennett, D. P., Fouqué, P., et al. 2006, *Nature*, 439, 437
- Bennett, D. P. 2010, *ApJ*, 716, 1408
- Bennett, D. P., & Rhie, S. H. 1996, *ApJ*, 472, 660
- Bennett, D. P., Bond, I. A., Udalski, A., et al. 2008, *ApJ*, 684, 663-683
- Bennett, D. P., Batista, V., Bond, I. A., et al. 2014, *ApJ*, 785, 155
- Bensby, T., Yee, J. C., Feltzing, S., et al. 2013, *A&A*, 549, A147
- Bond, I. A., Abe, F., Dodd, R. J., et al. 2001, *MNRAS*, 327, 868
- Bond, I. A., Bennett, D. P., Sumi, T., et al. 2017, *arXiv:1703.08639*
- Boyajian, T. S., van Belle, G., & von Braun, K. 2014, *AJ*, 147, 47
- Brown, T. M., Baliber, N., Bianco, F. B., et al. 2013, *PASP*, 125, 1031
- Burgasser, A. J., Kirkpatrick, J. D., Cruz, K. L., et al. 2006, *ApJS*, 166, 585
- Borucki, W. J., Koch, D. G., Basri, G., et al. 2011, *ApJ*, 736, 19
- Butler, R. P., Wright, J. T., Marcy, G. W., et al. 2006, *ApJ*, 646, 505
- Cassan, A., Kubas, D., Beaulieu, J.-P., et al. 2012, *Nature*, 481, 167
- Calchi Novati, S., Skowron, J., Jung, Y. K., et al. 2018, *arXiv:1803.04437*
- Choi, J.-Y., Shin, I.-G., Han, C., et al. 2012, *ApJ*, 756, 48
- Choi, J.-Y., Han, C., Udalski, A., et al. 2013, *ApJ*, 768, 129
- Claret, A. 2000, *A&A*, 363, 1081
- Claret, A., & Bloemen, S. 2011, *A&A*, 529, A75
- Dai, X., & Guerras, E. 2018, *ApJL*, 853, L27
- Dominik, M. 1999, *A&A*, 349, 108
- Doolin, S., & Blundell, K. M. 2011, *MNRAS*, 418, 2656
- Ford, E. B., & Rasio, F. A. 2008, *ApJ*, 686, 621-636
- Freeman, M., Philpott, L. C., Abe, F., et al. 2015, *ApJ*, 799, 181
- Fukui, A., Gould, A., Sumi, T., et al. 2015, *ApJ*, 809, 74
- Gaudi, B. S. 2012, *ARA&A*, 50, 411
- Gaudi, B. S., & Han, C. 2004, *ApJ*, 611, 528
- Gould, A. 1992, *ApJ*, 392, 442
- Gould, A., & Loeb, A. 1992, *ApJ*, 396, 104
- Gould, A., Dong, S., Gaudi, B. S., et al. 2010, *ApJ*, 720, 1073
- Gould, A., & Yee, J. C. 2014, *ApJ*, 784, 64
- Gould, A., Udalski, A., An, D., et al. 2006, *ApJL*, 644, L37
- Gould, A., Udalski, A., Monard, B., et al. 2009, *ApJL*, 698, L147
- Green, J., Schechter, P., Baltay, C., et al. 2012, *arXiv:1208.4012*
- Griest, K. & Safizadeh, N. 1998, *ApJ*, 500, 37
- Guillochon, J., Ramirez-Ruiz, E., & Lin, D. 2011, *ApJ*, 732, 74
- Han, C., & Gould, A. 1995, *ApJ*, 447, 53
- Han, C., Jung, Y. K., Udalski, A., et al. 2013, *ApJ*, 778, 38
- Han, C., Jung, Y. K., Udalski, A., et al. 2016, *ApJ*, 822, 75
- Han, C., Udalski, A., Sumi, T., et al. 2017, *ApJ*, 843, 59
- Holman, M. J., & Wiegert, P. A. 1999, *AJ*, 117, 621
- Holtzman, J. A., Watson, A. M., Baum, W. A., et al. 1998, *AJ*, 115, 1946
- Hwang, K.-H., Kim, H.-W., Kim, D.-J., et al. 2018, *arXiv:1802.10246*
- Ida, S., & Lin, D. N. C. 2005, *ApJ*, 626, 1045
- Jung, Y. K., Udalski, A., Sumi, T., et al. 2015, *ApJ*, 798, 123
- Kennedy, C. R., Beers, T. C., Marsteller, B., et al. 2006, *Bulletin of the American Astronomical Society*, 38, 168.11
- Kim, S.-L., Lee, C.-U., Park, B.-G., et al. 2016, *Journal of Korean Astronomical Society*, 49, 37
- Kim, D.-J., Kim, H.-W., Hwang, K.-H., et al. 2018, *AJ*, 155, 76
- Mao, S., & Paczynski, B. 1991, *ApJL*, 374, L37
- Pollack, J. B., Hubickyj, O., Bodenheimer, P., et al. 1996, *Icarus*, 124, 62
- Kaib, N. A., Raymond, S. N., & Duncan, M. 2013, *Nature*, 493, 381
- Kokubo, E., & Ida, S. 2002, *ApJ*, 581, 666

- Lecar, M., Podolak, M., Sasselov, D., & Chiang, E. 2006, *ApJ*, 640, 1115
- Levison, H. F., Lissauer, J. J., & Duncan, M. J. 1998, *AJ*, 116, 1998
- Liu, M. C., Dupuy, T. J., & Leggett, S. K. 2010, *ApJ*, 722, 311
- Luhman, K. L. 2012, *ARA&A*, 50, 65
- Luhman, K. L., Adame, L., D'Alessio, P., et al. 2005, *ApJL*, 635, L93
- Malmberg, D., Davies, M. B., & Heggie, D. C. 2011, *MNRAS*, 411, 859
- Mayor, M., & Queloz, D. 1995, *Nature*, 378, 355
- Mróz, P., Udalski, A., Skowron, J., et al. 2017, *Nature*, 548, 183
- Musielak, Z. E., Cuntz, M., Marshall, E. A., & Stuit, T. D. 2005, *A&A*, 434, 355
- Nataf, D. M., Gould, A., Fouqué, P., et al. 2013, *ApJ*, 769, 88
- Park, B.-G., Kim, S.-L., Lee, J. W., et al. 2012, *Proc. SPIE*, 8444, 844447
- Park, H., Han, C., Gould, A., et al. 2014, *ApJ*, 787, 71
- Ricci, L., Testi, L., Natta, A., Scholz, A., & de Gregorio-Monsalvo, I. 2012, *ApJL*, 761, L20
- Sako, T., Sekiguchi, T., Sasaki, M., et al. 2008, *Experimental Astronomy*, 22, 51
- Schechter, P. L., Mateo, M., & Saha, A. 1993, *PASP*, 105, 1342
- Shvartzvald, Y., Maoz, D., Udalski, A., et al. 2016, *MNRAS*, 457, 4089
- Skowron, J., Udalski, A., Kozłowski, S., et al. 2016, *AcA*, 66, 1
- Spergel, D., Gehrels, N., Breckinridge, J., et al. 2013, *arXiv:1305.5422*
- Street, R. A., Udalski, A., Calchi Novati, S., et al. 2016, *ApJ*, 819, 93
- Sumi, T., Abe, F., Bond, I. A., et al. 2003, *ApJ*, 591, 204
- Sumi, T., Bennett, D. P., Bond, I. A., et al. 2010, *ApJ*, 710, 1641
- Sumi, T., Kamiya, K., Bennett, D. P., et al. 2011, *Nature*, 473, 349
- Suzuki, D., Bennett, D. P., Sumi, T., et al. 2016, *ApJ*, 833, 145
- Szymański, M. K., Udalski, A., Soszyński, I., et al. 2011, *AcA*, 61, 83
- Thommes, E. W., Matsumura, S., & Rasio, F. A. 2008, *Science*, 321, 814
- Tomaney, A. B., & Crots, A. P. S. 1996, *AJ*, 112, 2872
- Udalski, A., Szymański, M. K., & Szymański, G. 2015, *AcA*, 65, 1
- Udalski, A., Ryu, Y.-H., Sajadian, S., et al. 2018, *arXiv:1802.02582*
- Veras, D., & Raymond, S. N. 2012, *MNRAS*, 421, L117
- Veras, D., & Tout, C. A. 2012, *MNRAS*, 422, 1648
- Veras, D., Wyatt, M. C., Mustill, A. J., Bonsor, A., & Eldridge, J. J. 2011, *MNRAS*, 417, 2104
- Verde, L., Peiris, H. V., Spergel, D. N., et al. 2003, *ApJS*, 148, 195
- Voyatzis, G., Hadjidemetriou, J. D., Veras, D., & Varvoglis, H. 2013, *MNRAS*, 430, 3383
- Wozniak, P. R. 2000, *AcA*, 50, 421
- Yee, J. C., Udalski, A., Sumi, T., et al. 2009, *ApJ*, 703, 2082
- Yee, J. C., Shvartzvald, Y., Gal-Yam, A., et al. 2012, *ApJ*, 755, 102
- Yoo, J., DePoy, D. L., Gal-Yam, A., et al. 2004, *ApJ*, 603, 139

Table 1. Data Sets for MOA-2015-BLG-337

Telescope	Diameter (m)	band	Number of data	k^1	e_{\min}^1
MOA-II	1.8	$R + I$	13813	1.081	0.003
		V	239	1.067	0.003
OGLE-IV	1.3	I	1754	1.247	0.003
B&C	0.61	g	124	0.898	0.003
		i	146	1.569	0.003
		r	145	1.009	0.003
KMTNet-SAAO	1.6	I	1555	1.576	0.003
KMTNet-SSO	1.6	I	1194	1.702	0.003
KMTNet-CTIO	1.6	I	2846	1.589	0.003

¹ The coefficients for error renormalization, see text.

Table 2. The Best-fit Model Parameters

Parameters	Units	Planetary	Planetary	Binary	Binary	BSPL
		(close)	(wide)	(close)	(wide)	
t_E	days	5.382(94)	5.432(90)	5.496(95)	6.104(99)	6.052
t_0	HJD-2450000	7214.9183(20)	7214.9243(23)	7214.9120(21)	7215.7390(21)	7215.0536
u_0		0.0470(11)	0.0567(18)	0.0458(12)	0.0435(13)	0.0331
q		0.0108(14)	0.0109(12)	0.178(23)	0.235(54)	-
s		0.606(33)	1.548(64)	0.263(11)	4.71(38)	-
α	radian	1.4445(57)	1.4449(63)	2.5359(78)	0.5877(75)	-
ρ		0.0223(30)	0.0263(23)	0.0166(< 0.0183) ^a	0.0152(< 0.0176) ^a	0.0041
$t_{0,2}^b$	HJD-2450000	-	-	-	-	7214.7049
$u_{0,2}^b$		-	-	-	-	0.0379
ρ_2^b		-	-	-	-	0.0048
fit χ^2		21800.18	21800.34	21806.26	21808.21	21852.51

NOTE—The numbers in parentheses indicate the 1σ uncertainties derived from the 16th/84th percentile values of the stationary distributions given by MCMC.

^a This value indicates a 1σ upper limit on ρ . The binary model including the parameter ρ is favored over one without ρ by only $\Delta\chi^2 < 4$. This indicates that the finite source effects for the binary models are not significant for fitting, and it's questionable to accept this ρ value directly. Thus, we do not adopt the best-fit ρ value but put an upper limit on ρ .

^b These are secondary source parameters for binary-source point-lens (BSPL) model.

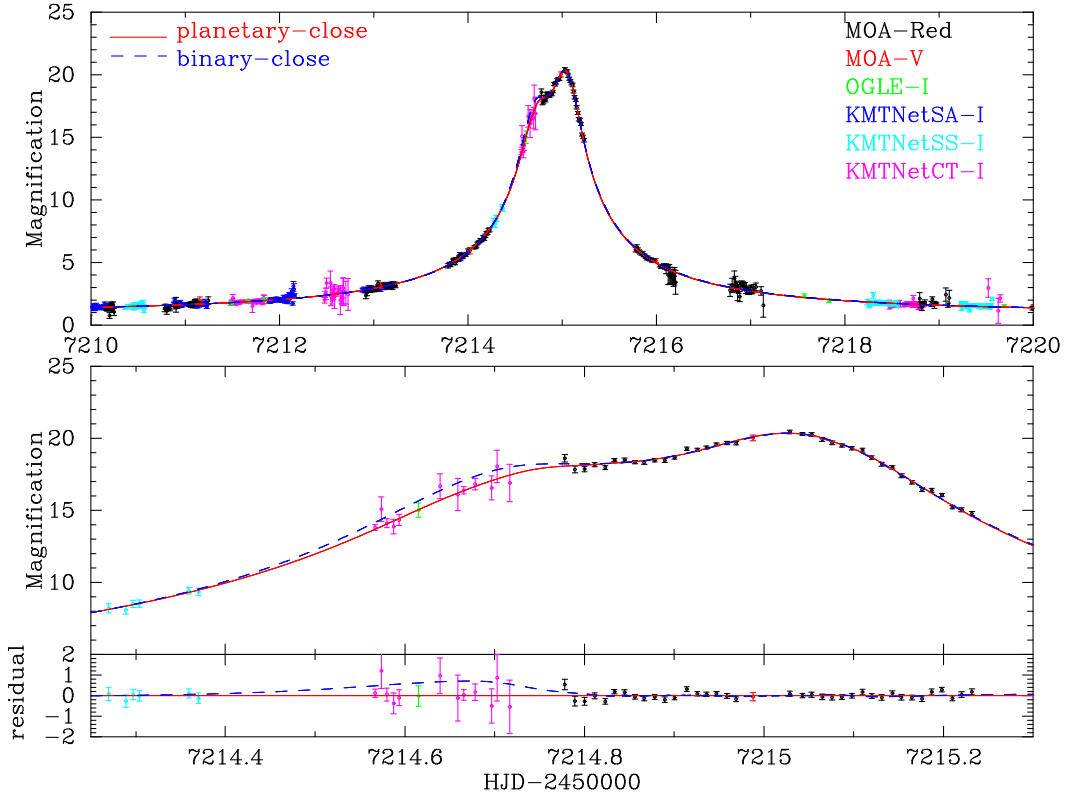


Figure 1. The light curve of MOA-2015-BLG-337. The top, middle and bottom panels show the entire period of the event, close-up of the anomaly and the residual from the best fitting planetary-close model, respectively. The red solid line and blue dashed line indicate the best planetary-close model and the best binary-close model. The binary model deviates from the planetary model particularly between $7214.5 < \text{HJD} - 2450000 < 7214.8$. The large photometric uncertainties in this period make it difficult to distinguish which is the best-fit model. The B&C data are not shown for clarity because of their large error bars while these data are used in the analysis.

Table 3. The Source Magnitude, Color and Angular Radius

	I (mag)	$V - I$ (mag)	θ_* (mas)
Source (measured from the light curve)	19.682 ± 0.012	1.611 ± 0.019	
Source ¹ (intrinsic)	18.478 ± 0.064	0.621 ± 0.074	0.621 ± 0.045
Source ² (intrinsic)	18.598 ± 0.064	0.720 ± 0.074	0.606 ± 0.045

¹This value is obtained by assuming the source suffered from the same extinction and reddening for the RCG.

²This value is obtained by assuming the source suffered from the extinction and reddening of 0.9 times as much as that for the RCG.

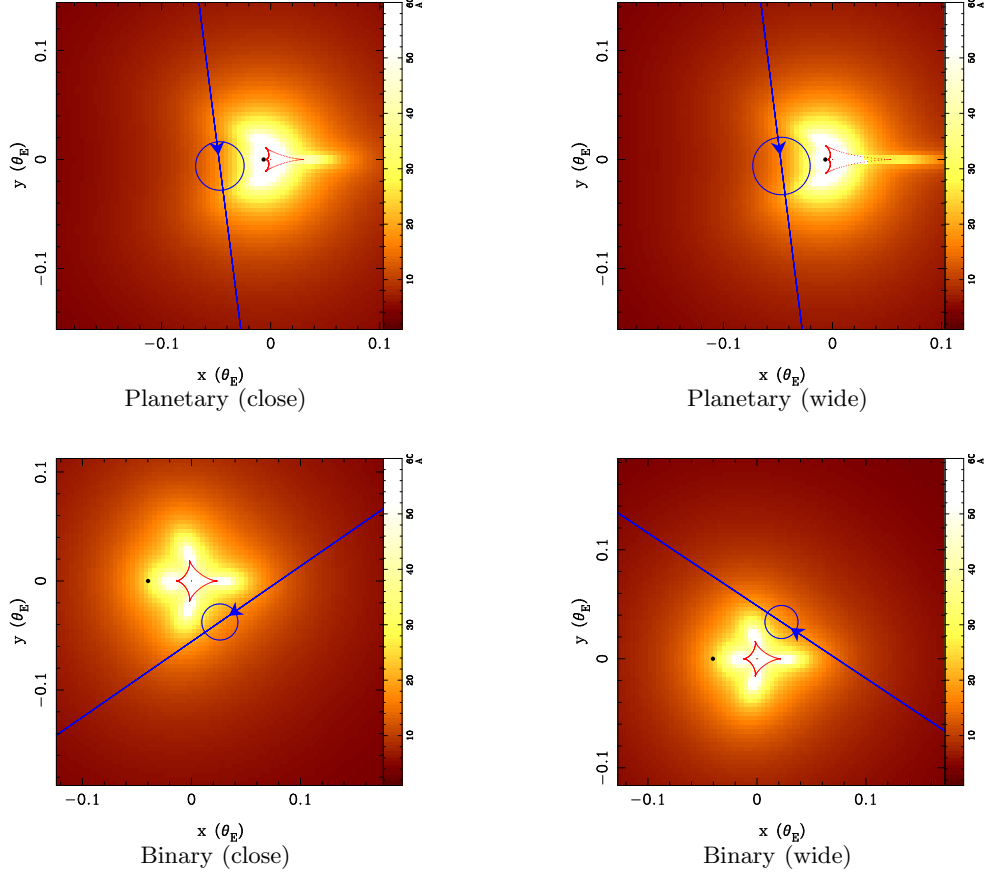


Figure 2. Caustic geometries for each model are shown as the red curves, respectively. The magnification patterns around them are also represented as contour maps. The brighter tone denotes higher magnifications. The blue lines show the source star trajectory with respect to the lens system, with the arrows indicating the direction of motion. The blue circles on the lines indicate the size of the source.

Table 4. Lens Properties derived from the Bayesian analysis with $\alpha_{bd} = 0.49$

Lens Parameters	$M_{\min} = 0.01$		$M_{\min} = 0.001$	
	Planetary	Binary ($s < 1$) ($s > 1$)	Planetary	Binary ($s < 1$) ($s > 1$)
M_{host}	$29.3^{+59.2}_{-15.4} M_{\text{Jup}}$	$78.0^{+131.0}_{-46.0} M_{\text{Jup}}$	$9.8^{+37.6}_{-6.8} M_{\text{Jup}}$	$78.5^{+133.1}_{-48.0} M_{\text{Jup}}$
M_{comp}	$100.7^{+203.0}_{-52.9} M_{\oplus}$	$18.3^{+30.8}_{-10.8} M_{\text{Jup}}$	$33.7^{+129.0}_{-23.2} M_{\oplus}$	$14.0^{+23.8}_{-8.6} M_{\text{Jup}}$
r_{\perp}	$0.26^{+0.06}_{-0.08} \text{ AU}$	$0.19^{+0.07}_{-0.06} \text{ AU}$ $3.3^{+1.2}_{-1.1} \text{ AU}$	$0.24^{+0.06}_{-0.09} \text{ AU}$	$0.19^{+0.07}_{-0.06} \text{ AU}$ $3.4^{+1.3}_{-1.1} \text{ AU}$
D_L	$7.5^{+1.1}_{-1.0} \text{ kpc}$	$6.3^{+1.2}_{-1.3} \text{ kpc}$	$7.1^{+1.1}_{-1.0} \text{ kpc}$	$6.3^{+1.2}_{-1.3} \text{ kpc}$

NOTE— These results are obtained by equation (3) with $\alpha_{bd} = 0.49$ and $M_{\text{break}} = 0.7$ as a prior initial mass function (IMF). In this function, the abundance ratio of main sequence stars, brown dwarfs and planetary objects is 1:0.72:0.27.

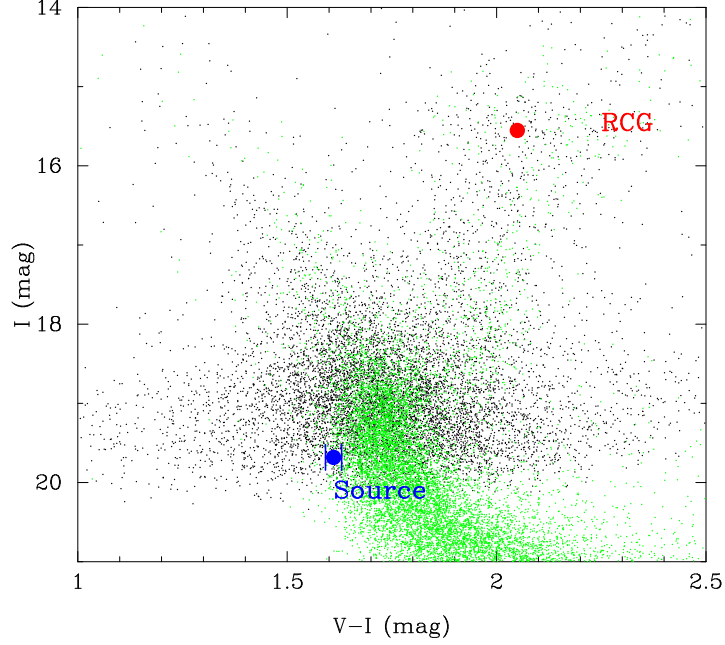


Figure 3. Color Magnitude Diagram (CMD) of OGLE-III stars within 2' of MOA-2015-BLG-337 (Black dots). The green dots indicate the Hubble Space Telescope (HST) CMD in Baade's window (Holtzman et al. 1998) whose color and magnitude are matched by using the RCG position. The red point indicates the centroid of red clump giant in this field, and the blue point indicates the source star in this event.

Table 5. Lens Properties derived from the Bayesian analysis with $\alpha_{\text{bd}} = 0.8$

Lens Parameters	$M_{\text{min}} = 0.01$		$M_{\text{min}} = 0.001$			
	Planetary	Binary		Planetary	Binary	
		($s < 1$)	($s > 1$)		($s < 1$)	($s > 1$)
M_{host}	$23.7^{+45.8}_{-10.7} M_{\text{Jup}}$	$67.5^{+120.0}_{-41.1} M_{\text{Jup}}$		$6.3^{+19.6}_{-3.9} M_{\text{Jup}}$	$63.8^{+116.7}_{-41.5} M_{\text{Jup}}$	
M_{comp}	$81.3^{+157.2}_{-36.7} M_{\oplus}$	$12.0^{+21.4}_{-7.3} M_{\text{Jup}}$		$21.6^{+67.3}_{-13.4} M_{\oplus}$	$11.4^{+20.8}_{-7.4} M_{\text{Jup}}$	
r_{\perp}	$0.26^{+0.06}_{-0.07} \text{ AU}$	$0.18^{+0.07}_{-0.06} \text{ AU}$	$3.2^{+1.3}_{-1.0} \text{ AU}$	$0.23^{+0.06}_{-0.08} \text{ AU}$	$0.17^{+0.07}_{-0.06} \text{ AU}$	$3.2^{+1.3}_{-1.0} \text{ AU}$
D_{L}	$7.5^{+1.1}_{-1.0} \text{ kpc}$	$6.2^{+1.2}_{-1.3} \text{ kpc}$		$7.0^{+1.1}_{-1.0} \text{ kpc}$	$6.2^{+1.2}_{-1.4} \text{ kpc}$	

NOTE— These results are obtained by equation (3) with $\alpha_{\text{bd}} = 0.8$ and $M_{\text{break}} = 0.5$ as a prior IMF. In this function, the abundance ratio of main sequence stars, brown dwarfs and planetary objects is 1:0.99:0.71.

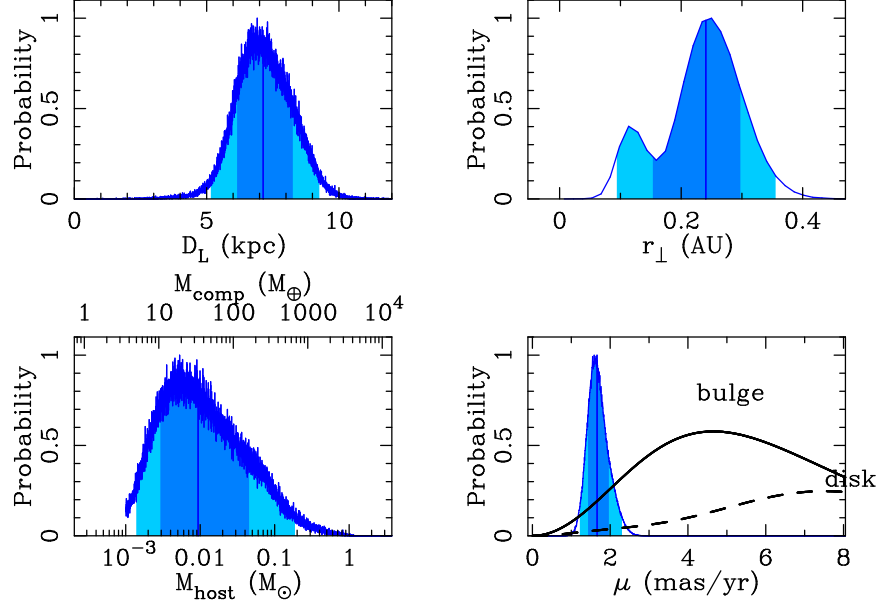


Figure 4. Probability distribution of lens properties for the **planetary** model derived from the Bayesian analysis with applying equation (3) with $\alpha_{\text{bd}} = 0.49$, $M_{\text{break}} = 0.7$ and $M_{\text{min}} = 0.001$. The dark and light blue regions indicate the 68.3% and 95.4% confidence interval, and the vertical blue lines indicates the median value. The right bottom panel shows the probability distribution for the lens-source relative proper motion μ , and the black line and the black dashed line indicate the prior μ probability distribution for Galactic bulge and disk, derived from the Galactic model (Han & Gould 1995)

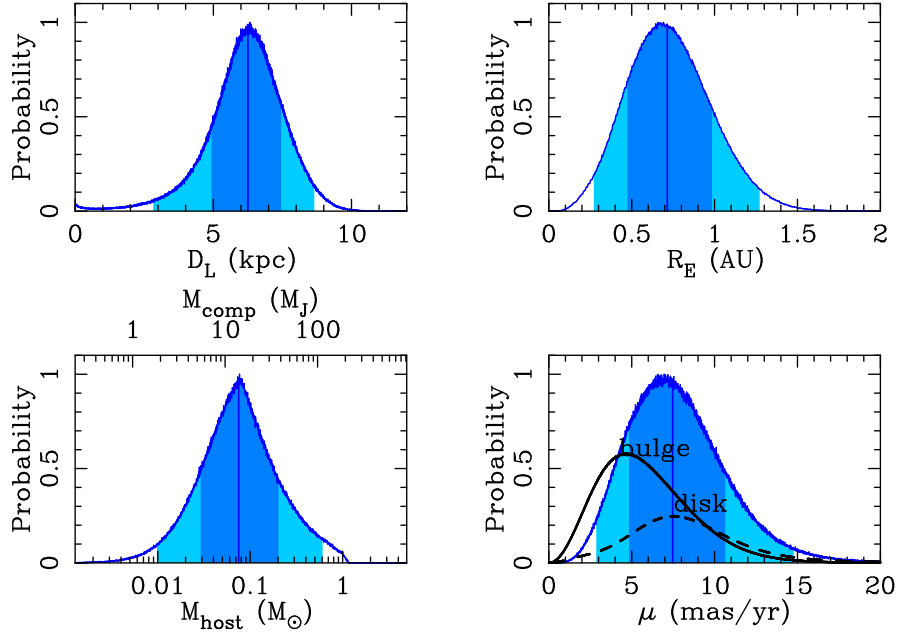


Figure 5. Probability distribution of lens properties for the **binary** model derived from the Bayesian analysis with applying equation (3) with $\alpha_{\text{bd}} = 0.49$, $M_{\text{break}} = 0.7$ and $M_{\text{min}} = 0.001$. The dark and light blue regions indicate the 68.3% and 95.4% confidence interval, and the vertical blue lines indicates the median value. The right bottom panel shows the probability distribution for the lens-source proper motion μ , and the black line and the black dashed line indicate the prior μ probability distribution for Galactic bulge and disk, derived from the Galactic model (Han & Gould 1995) .

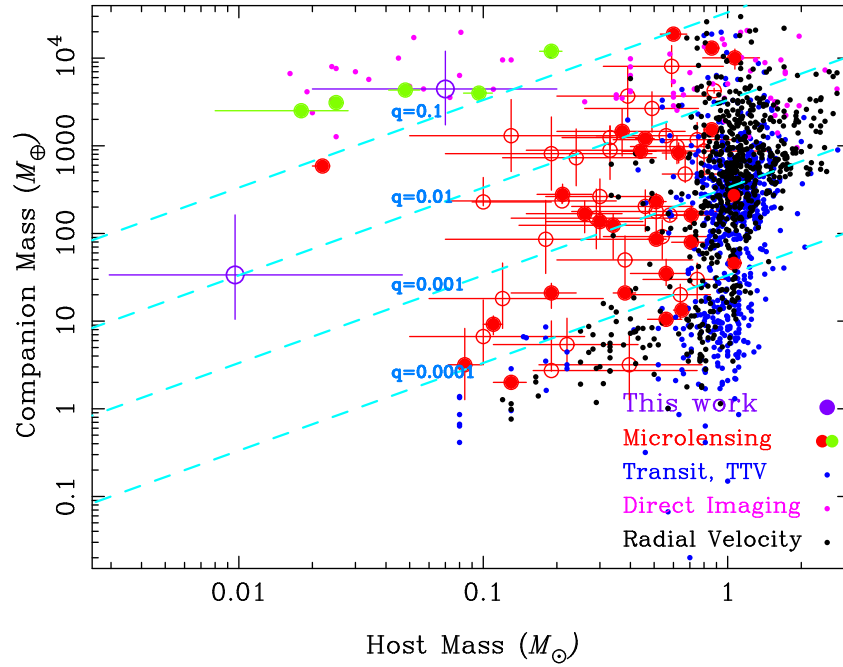


Figure 6. Distribution of bound exoplanets and very low mass companions in which the vertical axis shows the companion masses and the horizontal axis shows the host masses. The two purple points indicates the results of the Bayesian analysis for MOA-2015-BLG-337. The red, green, blue, magenta and black points indicate the planetary systems found by Microlensing (with a mass ratio of planet/host of $q < 0.1$), Microlensing ($q > 0.1$), Transit & TTV, Direct Imaging, and Radial Velocity, respectively. For the microlensing planets, filled circles indicate that their masses are measured and open circles indicate that their masses are estimated by a Bayesian analysis. The values of microlensing planets are from each discovery paper, while those of the others are from <http://exoplanet.eu>.